The fate of iron during hydration of white Portland cement-fayalitic slag

FENG, Jianhang, ZHANG, Minggen, EALES, James, SHEN, Siyi, YIO, Marcus, KATHYOLA, Thokozile, PONTIKES, Yiannis, BINGHAM, Paul <http://orcid.org/0000-0001-6017-0798> and MYERS, Rupert J

Cement and Concrete Research 208 (2026) 108324

Contents lists available at ScienceDirect

Cement and Concrete Research

journal homepage: www.elsevier.com/locate/cemconres

The fate of iron during hydration of white Portland cement-fayalitic slag

Jianhang Feng [a], Minggen Zhang [a], James Eales [b], Siyi Shen [a], Marcus Yio [a], Thokozile Kathyola [c], Yiannis Pontikes [d], Paul A. Bingham [b], Rupert J. Myers [a,*]

[a] Department of Civil and Environmental Engineering, Imperial College London, London, SW7 2AZ, United Kingdom
[b] Materials and Engineering Research Institute, College of Business, Technology and Engineering, Sheffield Hallam University, Sheffield, S1 1WB, United Kingdom
[c] Diamond Light Source, Didcot, Oxfordshire, OX11 0DE, United Kingdom
[d] KU Leuven, Department of Materials Engineering, 3001, Leuven, Belgium

ARTICLE INFO

Keywords:
FeO
Hydration
Fayalitic slag
White cement
Fe-rich cement

ABSTRACT

There is increasing interest in using Fe-rich materials in cement, yet the Fe speciation in hydrated cement paste remains poorly understood. This study quantitatively investigates the fate of amorphous Fe in hydrated white Portland cement-fayalitic slag pastes with varying Fe contents cured for 3, 28, and 90 days. The results show that Fe precipitated as ferrihydrite and potentially adsorbed on calcium (alumino)silicate hydrate (C-(A)-S-H) after 3 days of hydration. Afterwards, Fe stabilised in Fe-siliceous hydrogarnet and Fe-adsorbed C-(A)-S-H phases, accounting for ~15% and ~ 85% of total reacted Fe, respectively, after hydration for 90 days. The high Fe uptake by C-(A)-S-H was mainly attributed to Fe(III) adsorption rather than Fe(II). Thermodynamic modelling combined with microstructural analysis supported the predominant distribution of Fe on the C-(A)-S-H phase. These findings can advance understanding in using reactive Fe-containing materials in Portland cement pastes and the development of their chemical and physical properties.

1. Introduction

The rapid pace of population growth and urbanisation has driven extensive infrastructure development, resulting in significant demand for construction materials. Concrete, known for its low cost, adjustable strength, and durability, is one of the most widely used civil engineering materials, with global annual production of 17–22 billion tonnes [1]. However, its massive scale of production leads to the consumption of ~20 billion tonnes of natural resources annually and ~ 7% of global CO_2 emissions [2–4], primarily due to the production of Portland clinker (hereafter 'clinker').

One of the primary strategies for mitigating the carbon footprint of clinker is the use of supplementary cementitious materials (SCMs), including natural pozzolans, calcined pozzolans, and industrial by-products and wastes, such as ashes, glasses, and slags [5–7]. Among these SCMs, Fe-rich SCMs, including Fe-rich clays, steel slag, non-ferrous metallurgy slag, and bauxite residues, present promising alternatives due to their substantial cumulative global production of ~750 million tonnes/year [8] and composition (SiO_2, Al_2O_3, and CaO) that is similar to that of clinker and conventional SCMs. Moreover, their use as partial replacements for Portland cement can enhance mechanical performance [9–11] without significantly compromising concrete durability (e.g. resistance to carbonation, water and chloride ingress) [9,12–15] provided that the replacement level and slag chemistry (e.g. bauxite residue) are optimised.

It has been shown that reactive phases like alite (Ca_3SiO_5) and amorphous phases can be formed in Fe-rich cementitious materials through processes such as vitrification [16] and mechanical/chemical activation [17,18]. A promising approach involves modifying electric arc furnace slag to develop an alite-rich phase composition similar to Portland cement clinker by (partially) replacing the lime-dolomite flux with recycled cement paste. This engineered electric arc furnace slag can potentially meet the standard specification for clinker while significantly reducing its carbon footprint [19].

A key distinction between traditional and Fe-rich SCMs, especially non-ferrous metallurgy slags and vitrified bauxite residue [20], lies in their high FeO contents; the total content is higher as Fe-rich phases either form part of the process residue or cannot be recovered, whereas

* Corresponding author.
E-mail addresses: j.feng@imperial.ac.uk (J. Feng), m.zhang22@imperial.ac.uk (M. Zhang), James.Eales@shu.ac.uk (J. Eales), siyi.shen23@imperial.ac.uk (S. Shen), marcus.yio@imperial.ac.uk (M. Yio), thokozile.kathyola@diamond.ac.uk (T. Kathyola), yiannis.pontikes@kuleuven.be (Y. Pontikes), P.A.Bingham@shu.ac.uk (P.A. Bingham), r.myers@imperial.ac.uk (R.J. Myers).

https://doi.org/10.1016/j.cemconres.2026.108324
Received 9 March 2026; Received in revised form 20 May 2026; Accepted 12 June 2026
Available online 17 June 2026

the Fe^{2+} oxidation state is due to the process requirement, i.e., low oxygen partial pressure. Knowledge of the phase assemblages produced by hydrating Fe-rich SCMs in composite Portland cement remains limited, restricting the establishment of correlations between hydration chemistry with macro-scale properties (e.g. mechanical properties and durability) and hence engineering the design of Fe-rich cement systems. While pure phases, including Fe-ettringite [21], Fe- mono/hemicarbonate [22], Fe-monosulfate [23], Fe-katoite, Fe-siliceous hydrogarnet [24], Mg-(Al, Fe)-layered double hydroxides (LDHs) [25,26], Fe-carbonates [4], ferrihydrite [27], goethite, lepidocrocite [28], and Fe-bearing calcium-silicate-hydrate [29–31], have been successfully synthesized under ambient conditions, they have rarely been clearly identified and characterised experimentally in hydrated cements. For example, in hydrated calcium aluminate cement blended with zinc slag, Fe was identified in Al-rich and intermixed gel phases containing Ca, Al, and Si, whilst Fe uptake in ettringite, strätlingite, or monosulfoaluminate was not evident [32,33]. In hydrated Portland cement blended with non-ferrous metallurgy slag, Fe was suggested to be in a mossbauerite-like (Fe, Mg)-Al-LDH phase [34,35] in addition to siliceous hydrogarnet [23], ferrihydrite, and calcium-silicate-hydrate [36]. The composition, crystal structure and morphology of this LDH phase remains poorly understood, including notably the role of Al in its formation. The limitations of previous research show the need for additional quantitative analysis of Fe-bearing hydration products in hydrated cement samples containing Fe-rich SCMs to more clearly determine their formation and compositions. A better understanding of these materials can inform the engineering of blended cements with Fe-rich SCMs, thereby modifying their hydration product assemblages and improving their overall performance.

This study focuses on quantitative analysis of the distribution of Fe in hydration products formed in a Fe(II)-containing fayalitic slag-white Portland cement (wPC) paste. The fayalitic slag was selected because of its high content of amorphous Fe, enabling a high dosage of Fe in hydrate phases. The use of wPC, with its low inherent Fe content, ensures that the Fe in the hydration products predominantly originates from the slag. The quantitative analysis can contribute to the understanding of the dissolution-precipitation of Fe from Fe-rich SCMs in hydrated blended wPC cements, thereby guiding their use in these systems.

2. Materials and methods

2.1. Raw materials

Fayalitic slag, wPC, and tap water were used to prepare blended cement pastes. The chemical and mineralogical compositions of wPC are shown in Tables 1 and 2, respectively. The amount of Fe_2O_3 in the wPC is as low as 0.33 wt%. The fayalitic slag used was synthesized by Siakati et al. [37]. It is mostly composed of FeO and SiO_2 (Table 1). The amorphous content in the slag is 85.6 wt%, and its crystalline phases are fayalite (14.3 wt%) and magnetite (0.1 wt%) (Table 2). The amount of Fe_2O_3 in the wPC is as low as 0.3 wt%.

The particle size distribution of the fayalitic slag spans approximately 1–35 μm (Fig. 1), with d_{10}, d_{50}, and d_{90} values are 0.9, 6.8, and 32.2 μm, respectively, and a Blaine specific surface area of the fayalitic slag is 4140 cm^2/g [37]. The wPC shows a broader size range, from 0.1 to below 90 μm, with d_{10}, d_{50} and d_{90} values of 2.1, 10.1 and 30.7 μm, respectively.

Table 2
Mineralogical composition of the wPC and fayalitic slag precursors used here.

Phases	Formula	White cement (wt%)	Fayalitic slag (wt%)
C_3S	Ca_3SiO_5	71.9	
β-C_2S	Ca_2SiO_4	11	
γ-C_2S	Ca_2SiO_4	4.9	
C_3A	$Ca_3Al_2O_6$	3.8	
C_4AF	$Ca_2(Fe, Al)_2O_5$	2.3	
Gypsum	$CaSO_4•2H_2O$	2.5	
Dolomite	$CaMg(CO_3)_2$	1.9	
Calcite	$CaCO_3$	0.5	
Lime	CaO	0.4	
Thenardite	Na_2SO_4	0.4	
Periclase	MgO	0.4	
Fayalite	Fe_2SiO_4		14.3
Magnetite	Fe_3O_4		0.1
Amorphous			85.6

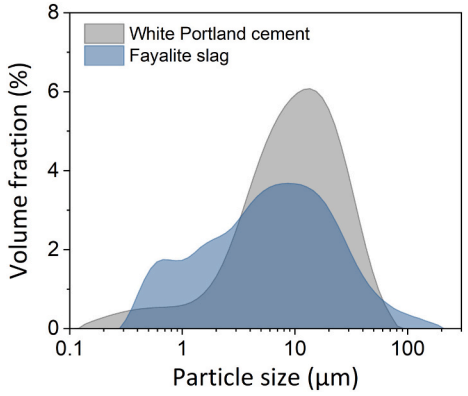

Fig. 1. Particle size distributions of the wPC and fayalitic slag.

2.2. Preparation of the white cement-fayalitic slag paste

To investigate the fate of amorphous Fe in hydrated cement paste, samples were prepared with systematically varied fayalitic slag contents such that FeO from the slag amorphous phase corresponded to 10 wt%, 20 wt%, and 30 wt% of the binders, alongside a reference paste of pure wPC. The FeO content was selected based on the reported FeO_x concentrations in Fe-rich clinkers (e.g. electric arc furnace clinker) [38–40] and in Portland cement blended with Fe-rich SCMs [14,34,35]. The corresponding proportions of wPC and fayalitic slag added into these samples are shown in Table 3. The water-to-binder mass ratio (w/b) was maintained at 0.5.

To prepare cement paste samples, wPC and fayalitic slag powders were dry-mixed for 10 min before water was added and blended for

Table 1
Chemical composition of the wPC and fayalitic slag.

Raw materials	Composition (wt%)											
	Na_2O	MgO	Al_2O_3	SiO_2	P_2O_5	SO_3	K_2O	CaO	TiO_2	Fe_2O_3[a]/FeO[b]	Others	LOI[c]/GOI[d]
White cement	0.1	0.5	2.2	25.0	0.3	1.8	0.1	69.0	0.1	0.3	0.3	0.3
Fayalitic slag	–	–	–	33.0	–	–	–	–	–	65.6	1.4	−8.0

[a] Fe_2O_3 in the white cement.
[b] FeO in the fayalitic slag, but minor amounts of Fe^{3+} are also expected to be present.
[c] Loss on ignition.
[d] Gain on ignition.

Table 3
Mixture proportions of wPC, and wPC-fayalitic slag systems.

Mixture	Description	wPC (wt% in the binder)	Fayalitic slag (wt% in the binder)	w/b
WC	White cement paste	100.0	0.0	0.5
10FeO	10 wt% FeO from the slag amorphous phase in the binder	82.0	18.0	
20FeO	20 wt% FeO from the slag amorphous phase in the binder	63.9	36.1	
30FeO	30 wt% FeO from the slag amorphous phase in the binder	45.9	54.1	

another 15 min. The mixture was cast into 20 × 20 × 20 mm^3 steel moulds which were subsequently covered with plastic film to prevent water evaporation. The covered samples were cured in air for 1 day, then demoulded and further cured in N_2-filled sealed bags at 23 °C for 3, 28, and 90 days to minimize oxidation of ferrous iron from air exposure, hence the speciation alterations of Fe upon hydration can be better analysed.

To stop hydration, samples were crushed, then immersed in isopropanol immediately for 15 min, after which the isopropanol was removed by filtration, and the residues were rinsed with isopropanol and diethyl ether for 1 and 2 times, respectively, as recommended by [41]. The residual samples were then dried at 40 °C in an oven for 8 min, then stored in a desiccator under low vacuum (~2 × 10^4 Pa) before analysis. Neither solvent exchange nor oven drying can fully prevent exposure of the samples to atmospheric oxygen, potentially resulting in slight oxidation.

2.3. Characterization of the wPC-fayalitic slag paste

Fourier-transform infrared spectroscopy (FTIR) was performed on the hydrated blended cement paste. Anhydrous white cement and fayalitic slag were also analysed for comparison. The samples ground into powders below 63 μm were placed against an ATR crystal of an FTIR analyzer (Nicolet iS50, Thermo Scientific) and scanned in the wavenumber range of 4000–400 cm^{-1} at a step size of 1 cm^{-1} for 40 times after background scans were collected.

Thermogravimetric analysis (TGA) was conducted on the dried hydrated samples from 30 to 900 °C at a heating rate of 10 °C/min under nitrogen flow by using a thermal analyzer (STA 449, NETZSCH). Dehydroxylation and decarbonation of samples were estimated using the tangential method by calculating the mass loss within temperature ranges of 400–550 °C and 600–800 °C respectively. The H_2O and CO_2 mass losses from the samples were further used to calculate X-ray mass absorption coefficients during X-ray diffraction analysis.

X-ray diffraction (XRD) was applied to analyze the crystalline phase assemblage and reaction degree of fayalitic slag in hydrated white cement-fayalitic slag paste. The dried samples were ground into powders with particle size below 63 μm then backloaded into sample holders which were mounted on a spinning stage and scanned over an angular range of 5 to 80° 2θ using CoKα radiation on an X-ray diffractometer (Empyrean, Malven Panalytical) at 45 kV and 40 mA. Quantitative XRD (QXRD) analysis was performed by Rietveld refinement in Highscore Plus v4.1a software. Corundum (Aluminium oxide, ≥99.70%, Thermo scientific) was used as the external standard to calculate the G-factor [42]. R-Bragg (R_B) factor calculated by using Eq. (1) [43,44] was used as the criterion of Rietveld refinement for each individual phase. The chemical compositions of white cement and fayalitic slag, as shown in Table 1, were combined with TGA results to determine the X-ray mass absorption coefficients of these hydrated paste samples. The uncertainties in quantitative XRD and R_B factors were determined based on 3 replicates.

$$R_B = \frac{\sum_K |I_K - I_{cK}|}{\sum_K I_K} \quad (1)$$

where R_B denotes the R-Bragg factor; I_K denotes the observed intensity of the K^{th} Brag reflection; I_{cK} denotes the calculated intensity of the K^{th} Brag reflection.

Backscattered electron (BSE) imaging analysis coupled with energy dispersive spectroscopy (EDS) was carried out to identify the Fe-bearing hydration products and determine Fe adsorption on C-(A)-S-H. The ~1 mm dried cement paste samples obtained by breaking the bulk paste into pieces were impregnated in epoxy resin, ground using SiC papers (120, 220, 500, 1000 and 1200 grit sizes) and polished on cloths embedded with diamond abrasives (9, 6, 3, 1 and 0.25 μm), according to the method in [45]. The polished samples were washed ultrasonically in acetone after each grinding and polishing step. The prepared samples were carbon-coated and then observed at a backscattered mode under a 20 kV accelerating voltage and an 8.5 mm free working distance by using a scanning electron microscope (Sigma 500 VP, Zeiss) equipped with an energy dispersive spectrometer (X-Max 150, Oxford Instruments). Due to the high Fe Kα critical excitation energy of 7.1 keV, the relatively high accelerating voltage is selected to reach an accelerating voltage to Fe Kα critical excitation energy ratio of 2.8, which is close to the optimal ratio (~2.7) as recommended in [46].

To analyze Fe-bearing hydration products and Fe adsorbed on C-(A)-S-H, EDS mapping, point and line analysis were carried out. The EDS maps were collected at a resolution of 4096 × 3072 pixels with a dwell time of 512 μs. The EDS mapping data were then quantified with the built-in standard database using the AZtec software. The EDS data points were collected at a total number of X-ray counts of 50,000. The Fe/Si atomic ratios were calculated from data points with Si/Ca atomic ratios within one standard deviation of the Si/Ca ratio of C-(A)-S-H, which is determined according to the method in [47]. The Welch's *t*-test was performed to assess differences in Fe/Si atomic ratios between inner and outer C-(A)-S-H. The EDS line data were collected at a point density of 256 from inside slag particles to the hydrated cement paste.

^{57}Fe Mössbauer spectroscopy measurements were acquired using acrylic absorber discs containing tens of milligrams of powdered sample spread over an area of 1.767 cm^2. The absorber discs were loaded to present an Fe areal density of up to 2.16 × 10^{-3} g/cm^2 and achieve a Mössbauer thickness of 1 [48,49] by diluting each specimen according to its iron content. The 14.4 keV γ-rays were supplied by the cascade decay of 25 mCi ^{57}Co in a Rh matrix source and were oscillated at constant acceleration with a velocity range of ±12 mm/s. All measurements were performed at 296 ± 2 K. All spectra were calibrated relative to α-Fe foil at room temperature. Spectral fitting was carried out using the Recoil software package [50], adopting a Lorentzian-based fitting approach.

Fe K-edge X-absorption spectroscopy (XAS) analysis was performed at beamline B18 (Diamond Light Source, UK) using Si (111) double-crystal monochromator [51]. The synchrotron was operated at 3 GeV with a ring current of 300 mA. XAS was used to quantify the proportions of Fe in different phases of the hydrated wPC-fayalitic slag paste. The cement pastes and references, including fayalitic slag, Fe-siliceous hydrogarnet ($C_3FS_{1.34}H_{3.32}$, $C_3(A_{0.5}F_{0.5})S_{0.84}H_{3.32}$), 2-line, 6-line and siliceous ferrihydrite ($(Fe_2O_3)_{0.97}SiO_2(H_2O)_{2.81}$, $Fe_2O_3(SiO_2)_{0.74}(H_2O)_{2.36}$), were diluted using powdered cellulose, lightly pressed into thin pellets and sealed between Kapton films. Each sample was scanned 3 times over the energy range 7012–8092 eV in transmission mode at room temperature.

Energy calibration was conducted by assigning the energy of Fe K-edge (7112 eV) to the first inflection point of Fe foil XAS spectrum. The spectra of each sample were merged and normalised using Athena from the Demeter software package [52]. Least-square linear combination fitting (LCF) was carried out on the X-ray absorption near edge structure

(XANES) region from 20 eV below to 80 eV above the Fe K-edge. The spectra from reference samples and Fe(II)/Fe(III)-adsorbed calcium-silicate-hydrate (C-S-H) in [29,30] were used for the LCF analysis and all the weights of reference spectra were constrained between 0 and 1. The goodness of fit was assessed by using the R-factor calculated according to Eq. (2).

$$R = \sum \frac{(I_{obs} - I_{cal})^2}{N} \quad (2)$$

where R denotes the residual factor; I_{obs} denotes the observed normalised intensities; I_{cal} denotes the calculated normalised intensities; N denotes the number of data points.

2.4. Thermodynamic modelling

Thermodynamic modelling was conducted using the Gibbs Energy Minimization software GEMS v3.7 [53] with PSI/Nagra [54] and Cemdata 18 databases [55]. Goethite, hematite and magnetite phases in the database were excluded from the simulations, as their formation in cement paste is kinetically hindered under ambient temperature and pressure. The C-(A)-S-H compositions were simulated by using the C-(N-)A-S-H solid solution model [56]. Fe adsorption on C-S-H was set based on the Fe/Ca and Fe/Si atomic ratios of outer C-(A)-S-H at slag/cement interface and cement matrix regions, respectively, due to the different phase assemblage at these regions. These atomic ratios were determined by EDS point analysis as introduced in Section 2.3. The Fe-siliceous hydrogarnet phases ($Ca_3(Al_xFe_{1-x})_2(SiO_4)_y(OH)_{4(3-y)}$) used for modelling were $C_3(A,F)S0.84H_{4.32}$ and $C_3FS_{1.34}H_{3.32}$, which are present in the Cemdata18 database. While Fe-siliceous hydrogarnet with silica content outside this range (i.e., $0 < y < 3$) is possible [24], these phases (i.e., $C_3(A,F)S0.84H_{4.32}$ and $C_3FS_{1.34}H_{3.32}$) fall within the silica content range of Fe-siliceous hydrogarnet observed in hydrated cement paste [23], so we use them here.

To model the distributions of hydration product phase assemblage in localized Fe-rich zones, EDS line analysis in Section 2.3 was applied to determine the chemical compositions around fayalitic slag particles, including CaO, SiO_2, Al_2O_3, MgO, SO_3, FeO and Na_2O. In order to determine the reacted FeO content of near-surface regions of the slag particles and given the high Fe content in fayalitic slag (65.6 wt%), hydration products within the regions of slag particles were assumed to be Fe-siliceous hydrogarnet ($Ca_3(Fe)_2(SiO_4)_y(OH)_{4(3-y)}$). On this basis, the CaO content was used to determine to the amount of Fe-siliceous hydrogarnet at near-surface slag regions. The reacted FeO content at the region was subsequently estimated by using the calculated Fe-siliceous hydrogarnet amount. By assuming congruent dissolution, the reacted SiO_2 content in the region was determined based on the FeO reaction degree, which was calculated by dividing the estimated reacted FeO content by the total FeO content from EDS analysis. For the hydrated cement paste area, the reaction degree of all components was set at 100%. The mass ratio of water-to-reacted components was 0.5. The environmental conditions for hydration were set to 25 °C and 1 bar.

3. Results and discussion

3.1. Reaction degree of fayalitic slag in wPC paste

The reaction degree of fayalitic slag after hydration of 28 and 90 days is determined by ^{57}Fe Mössbauer spectroscopy. The ^{57}Fe Mössbauer spectrum of the fayalitic slag (Fig. 2) was fitted with 2 doublets (D1 and D2) corresponding to ferrous ions [37] (Table 4). Given the wide range of local environments in amorphous networks typically lead to larger linewidth (Γ) than the well-defined bonds of crystals [57,58], the D2 doublet is more likely associated with the amorphous phase of the

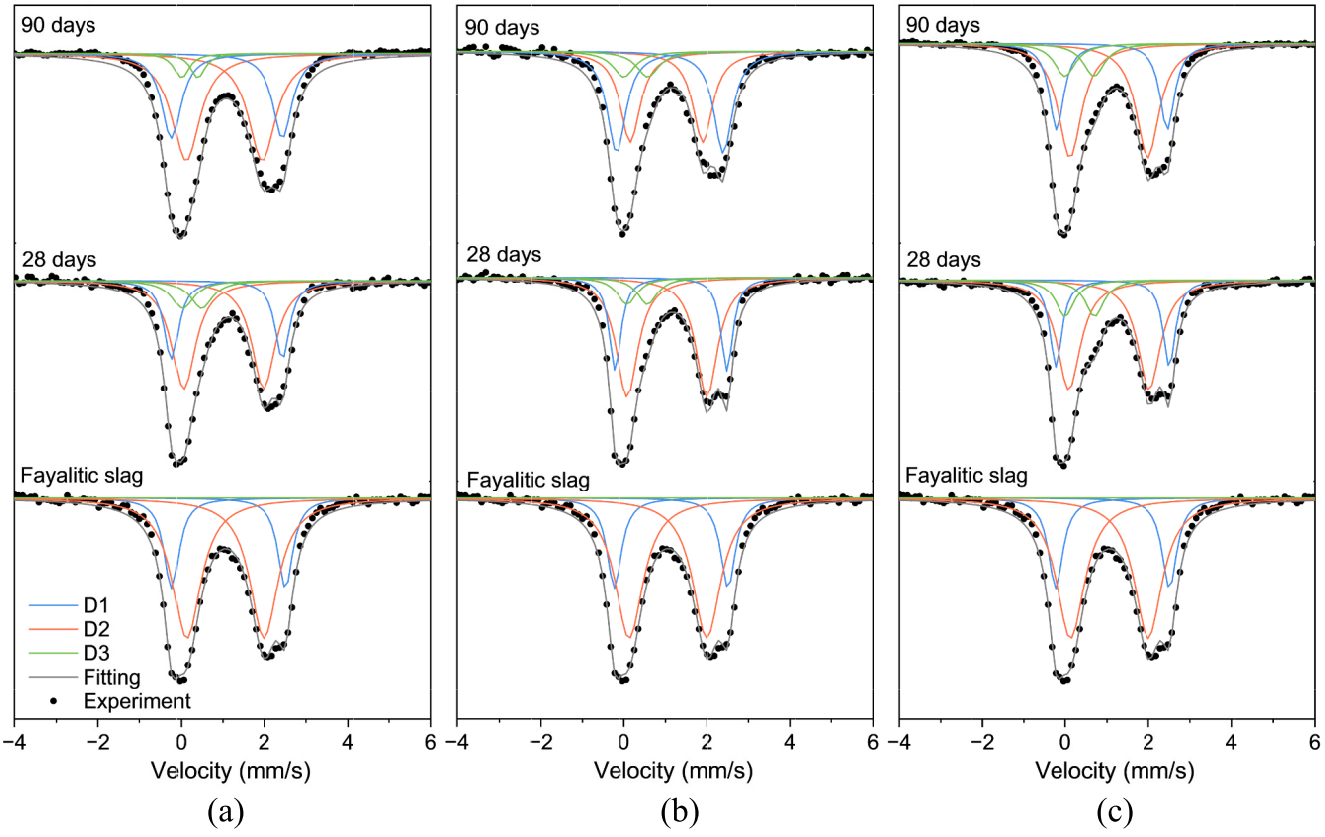

Fig. 2. ^{57}Fe Mössbauer spectra of raw fayalitic slag and 28 and 90-day hydrated cement paste with the binder containing (a) 10 wt%, (b) 20 wt%, and (c) 30 wt% FeO from the slag amorphous phase in the binder. D1, D2 and D3 are doublets for fitting the spectra. The fitting details can be seen in Table 4.

Table 4
^{57}Fe Mössbauer hyperfine parameters of components for fitting of the spectra of fayalitic slag, 28 and 90-day hydrated cement paste containing 10 wt%, 20 wt% and 30 wt% FeO from the slag amorphous phase in the binder. CS denotes the centreshift, QS denotes the quadrupole spilt, Γ denotes the half-width at half-maximum (HWHM), AA denotes the relative absorption area of the components. D denotes doublet. Calculated uncertainties are given in parentheses.

Sample	CS (mm/s)	QS (mm/s)	Γ (mm/s)	AA (%)	Component
Fayalitic slag	1.14	2.74	0.21	24.7	D1: Fe(II)
	(0.02)	(0.02)	(0.03)	(4.0)	
	1.06	1.87	0.41	75.3	D2: Fe(II)
	(0.02)	(0.04)	(0.02)	(4.5)	
28-day "10FeO" cement paste	1.10	2.67	0.21	26.0	D1: Fe(II)
	(0.02)	(0.03)	(0.03)	(5.8)	
	1.02	1.93	0.35	59.5	D2: Fe(II)
	(0.08)	(0.18)	(0.03)	(7.3)	
	0.26	0.45	0.33	14.4	D3: Fe(III)
	(0.31)	(0.60)	(0.09)	(2.3)	
90-day "10FeO" cement paste	1.10	2.67	0.28	32.7	D1: Fe(II)
	(0.02)	(0.03)	(0.02)	(4.2)	
	1.03	1.84	0.41	60.1	D2: Fe(II)
	(0.02)	(0.04)	(0.02)	(4.6)	
	0.20	0.38	0.21	7.2	D3: Fe(III)
	(0.03)	(0.05)	(0.04)	(2.0)	
28-day "20FeO" cement paste	1.14	2.70	0.17	25.9	D1: Fe(II)
	(0.02)	(0.02)	(0.02)	(2.7)	
	1.04	1.92	0.32	61.3	D2: Fe(II)
	(0.06)	(0.12)	(0.02)	(3.8)	
	0.32	0.49	0.29	12.7	D3: Fe(III)
	(0.24)	(0.47)	(0.06)	(2.0)	
90-day "20FeO" cement paste	1.11	2.57	0.27	42.5	D1: Fe(II)
	(0.02)	(0.02)	(0.02)	(2.0)	
	1.03	1.74	0.29	44.3	D2: Fe(II)
	(0.02)	(0.02)	(0.02)	(2.0)	
	0.29	0.58	0.32	13.2	D3: Fe(III)
	(0.03)	(0.06)	(0.05)	(2.3)	
28-day "30FeO" cement paste	1.14	2.73	0.18	24.6	D1: Fe(II)
	(0.02)	(0.02)	(0.02)	(2.4)	
	1.05	1.93	0.34	59.7	D2: Fe(II)
	(0.02)	(0.03)	(0.02)	(3.2)	
	0.35	0.71	0.29	15.8	D3: Fe(III)
	(0.03)	(0.07)	(0.03)	(2.0)	
90-day "30FeO" cement paste	1.12	2.67	0.22	27.3	D1: Fe(II)
	(0.02)	(0.02)	(0.02)	(2.1)	
	1.05	1.87	0.35	57.9	D2: Fe(II)
	(0.02)	(0.02)	(0.02)	(2.6)	
	0.34	0.70	0.31	14.8	D3: Fe(III)
	(0.02)	(0.06)	(0.03)	(2.0)	

fayalitic slag than D1. As the QXRD analysis suggested only a minor content of magnetite (0.1 wt%) in the fayalitic slag (Table 2), its contributions cannot be identified within these two doublets.

The ^{57}Fe Mössbauer spectra of the hydrated cement paste were fitted with 3 doublets (Table 4). The Fe(II)-related doublets (D1 and D2) showed CS and QS values similar to those of Q1 and Q2 in the fayalitic slag, suggesting they were attributed to unreacted fayalitic slag. Another doublet (D3) was related to Fe(III) and showed distinctly different hyperfine parameters to those of fayalitic slag, indicating its relation to the reaction products of fayalitic slag. Based on the relative area of D3, the reaction degree of fayalitic slag in "10FeO", "20FeO" and "30FeO" cement pastes after 28 days of hydration was estimated to be ~14 ± 2%, ~13 ± 2% and ~ 16 ± 2%, respectively. After hydration for 90 days, the increase in area fraction of D3 doublet in "20FeO" and "30FeO" was limited, compared with the spectra of their 28-day samples, indicating the limited reaction degree increase of fayalitic slag from 28 to 90 days. This is consistent with previous work [59], which shows that the increase in Fe reaction degree in fayalitic slag slows after 14 days of curing. The decrease in relative area of D3 of 10FeO group from 28 to 90 days of hydration could be associated with the fitting uncertainties. Three doublets were adopted to ensure fitting reliability; however, the single doublet D3 might not fully correspond to the complex assemblage of Fe-containing phases in the hydration products. Moreover, the evolution of Fe-bearing hydration products with curing age, as discussed in the following Sections 3.2 and 3.3, could alter the recoil-free fraction of Fe, such that the absorption area fractions do not accurately represent the exact atomic fractions of Fe at different sites [60]. These limitations led to uncertainties in the estimation of the reaction degree.

3.2. Fe-bearing hydration products

3.2.1. Fe adsorbed on C-(A)-S-H

BSE-EDS analysis of C-(A)-S-H indicates distinct Fe concentrations in inner and outer C-(A)-S-H. A typical result for the hydrated cement paste with 30 wt% FeO from the slag amorphous phase in the binder (45.88 wt % wPC, 54.12 wt% Fayalitic slag) after curing for 28 days is shown in Fig. 3. In Fig. 3 (a), regions where wPC clinker particles have completely dissolved are filled with typical 'inner' hydration products (C-(A)-S-H) and surrounded by 'outer' hydration products (both appear as dark grey regions), porosity (black regions), and fayalitic slag particles (light grey particles), as verified by the EDS mapping results in Fig. 3 (b-d). The Fe distribution inside and outside the fully hydrated cement particle is shown in Fig. 3 (b), revealing that the Fe concentrations in inner hydration products are much lower than in outer hydration products. Portlandite is located in the regions with the highest calcium concentrations (Fig. 3 (c)).

The distinction in the distribution of Fe in inner and outer hydration products is further supported by the EDS point analysis in Fig. 3 (e-g). These results show that there is limited intermixing of C-(A)-S-H with AFt and AFm. The inner and outer hydration products primarily consisted of C-(A)-S-H with similar Si/Ca (0.73 and 0.74 for the inner and outer products, respectively) and Al/Ca ratios (0.05 and 0.04, respectively), as shown in Fig. 3 (e), which is consistent with previous results [47,62]. However, the Fe/Ca ratios were much higher in outer C-(A)-S-H compared to inner C-(A)-S-H (Fig. 3 (f)), indicating greater Fe adsorption on the outer C-(A)-S-H. The needle-shaped C-(A)-S-H was identified around or on the surface of fayalitic slag particles, as shown in Fig. 4 (a-c).

Estimated Fe/Si atomic ratios from at least 150 points in inner and outer hydration products are summarized in Table 5. The Fe/Si atomic ratios of inner and outer C-(A)-S-H in the blended cement paste differed significantly ($p < 0.01$). The Fe/Si atomic ratios in outer C-(A)-S-H were higher than those in inner C-(A)-S-H, and both were significantly higher than the Fe/Si ratios in plain white cement paste, indicating adsorption of Fe originating from fayalitic slag particles in addition to the cement particles. These Fe/Si atomic ratios in C-(A)-S-H are comparable to those reported in previously hydrated cement paste studies [32,34,36,63]. Compared with Fe sorption in synthetic C-S-H [29,30], the Fe/Si atomic ratios in inner C-(A)-S-H in this study generally fall within the range of Fe(II) and Fe(III) sorption in synthetic C-S-H, whilst the Fe/Si atomic ratios in outer C-(A)-S-H exceeds the range for Fe(II) uptake but remains within the limit for Fe(III) adsorption in synthetic C-S-H. Given the higher Fe(III) than Fe(II) adsorption on C-S-H at equilibrium [29,30], the higher Fe adsorption on outer C-(A)-S-H could be relevant to the oxidation of Fe on outer hydration products. Additionally, the low solubility of Fe-hydroxides [64] and potential adsorption of Fe on fayalitic slag surfaces could limit the diffusion of Fe dissolved from the fayalitic slag [65,66], which could lead to the higher adsorption of Fe on outer than inner C-(A)-S-H.

Furthermore, the Fe adsorption on C-(A)-S-H increased with the fayalitic slag content in the blended cement paste, which could be due to higher dissolved Fe content in these samples at constant curing age (i.e., similar slag reaction degrees). We note that the increase in Fe adsorption on C-A-S-H was not linear with the increase of FeO content from the slag amorphous phase in hydrated cement paste, suggesting the Fe adsorption on C-(A)-S-H was also determined by wPC content. This could be attributed to variations in C-(A)-S-H content due to differences in wPC content in the cement paste, and reactions between Fe and hydration

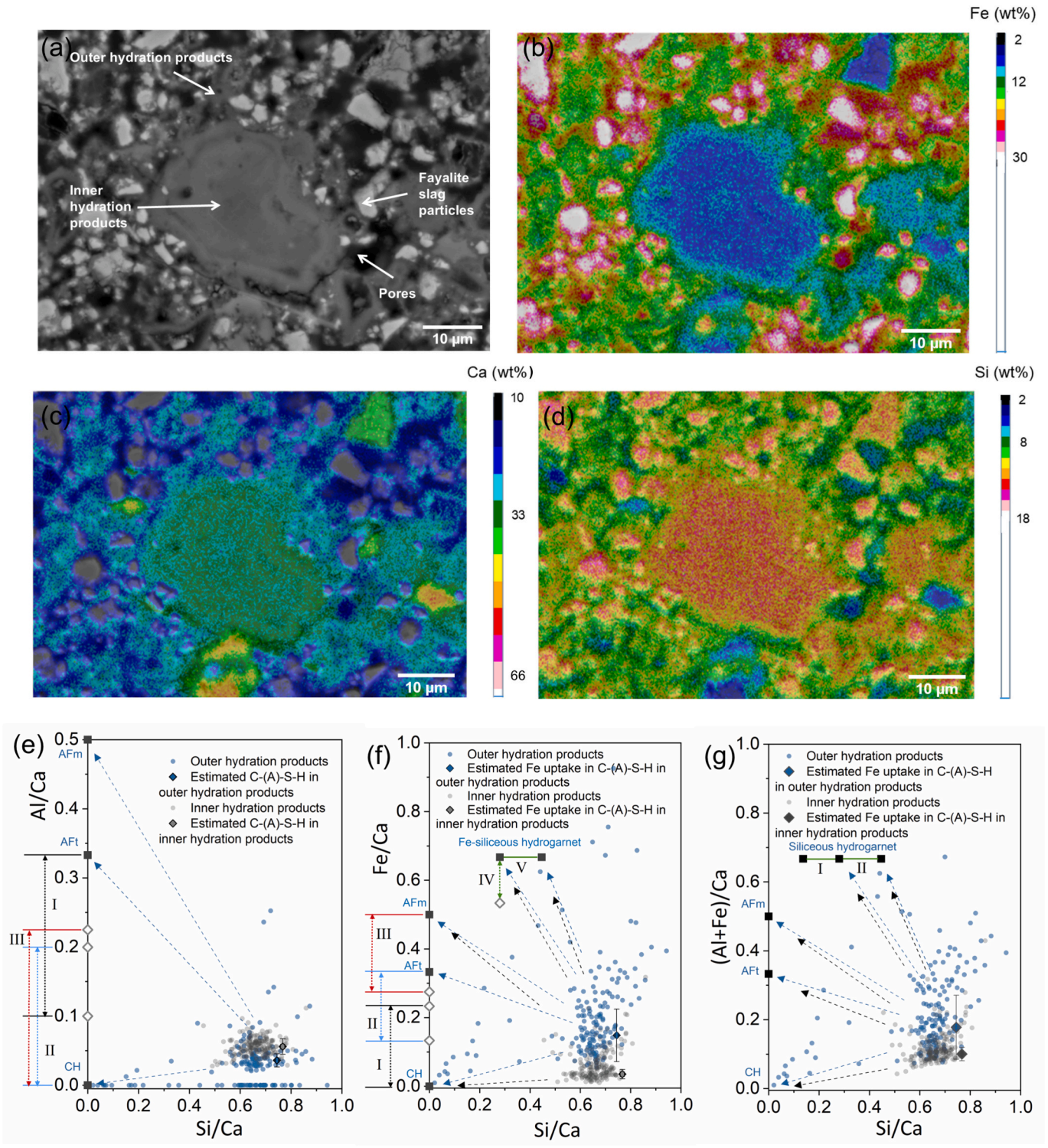

Fig. 3. BSE-EDS analysis at 28-days of hydration for cement paste containing 30 wt% FeO from the slag amorphous phase in the binder. (a) A BSE image of the sample; (b-d) EDS mappings of Fe, Ca and Si elements; (e) EDS point analysis of Al/Ca as a function of Si/Ca, **I** represents the Al/Ca range in Al-(Fe)-ettringite solid solution [21], **II** represents the Al/Ca range of Fe-(Al)-ettringite solid solution [21], and **III** represents the Al/Ca range of Fe-(Al)-monosulfate solid solution [61]; (f) Fe/Ca as a function of Si/Ca, **I** represents the Fe/Ca range in Al-(Fe)-ettringite solid solution [21], **II** represents the Fe/Ca range of Fe-(Al)-ettringite solid solution [21], **III** represents the Fe/Ca range of Fe-(Al)-monosulfate solid solution [61], **IV** represents the Fe/Ca range of Fe-(Al)-siliceous hydrogarnet solid solution, and **V** represents the Si/Ca range in the miscibility gap between $C_3FS_{0.84}H_{4.32}$ and $C_3FS_{1.34}H_{3.36}$ [24]; and (g) (Al + Fe)/Ca as a function of Si/Ca in inner and outer hydration products, **I** represents the Si/Ca range in miscibility gap between $C_3AS_{0.41}H_{5.18}$ and $C_3AS_{0.84}H_{4.32}$, **II** represents the Si/Ca range in miscibility gap between $C_3FS_{0.84}H_{4.32}$ and $C_3FS_{1.34}H_{3.36}$ [24].

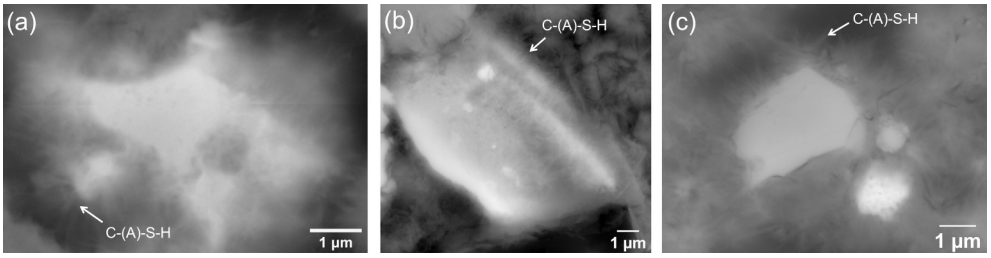

Fig. 4. BSE images of fayalitic slag in 90-day hydrated cements with the binder containing (a) 10 wt%, (b) 20 wt% and (c) 30 wt% FeO from the slag amorphous phase in the binder.

Table 5
Estimated Fe/Si atomic ratios by EDS analysis for inner and outer hydration products.

Curing age (days)	Mix group	Estimated Fe/Si in inner C-(A)-S-H	Estimated Fe/Si in outer C-(A)-S-H	p
3	WC	0.013 ± 0.0046	0.015 ± 0.0048	0.285
	10FeO	0.032 ± 0.0187	0.136 ± 0.0128	1.10×10^{-3}
	20FeO	0.096 ± 0.0359	0.366 ± 0.1681	2.41×10^{-6}
	30FeO	0.179 ± 0.0486	0.419 ± 0.1365	1.84×10^{-11}
28	WC	0.012 ± 0.0054	0.011 ± 0.0048	0.367
	10FeO	0.023 ± 0.0134	0.206 ± 0.1433	1.83×10^{-4}
	20FeO	0.023 ± 0.0049	0.386 ± 0.1831	3.22×10^{-11}
	30FeO	0.036 ± 0.0124	0.298 ± 0.1467	5.38×10^{-24}
90	WC	0.017 ± 0.0036	0.010 ± 0.0058	1.04×10^{-3}
	10FeO	0.023 ± 0.0072	0.110 ± 0.1030	6.93×10^{-4}
	20FeO	0.037 ± 0.0203	0.229 ± 0.1257	9.72×10^{-12}
	30FeO	0.082 ± 0.0334	0.457 ± 0.1476	1.05×10^{-14}

products of wPC, which is further investigated in the following sections.

3.2.2. *Fe-siliceous hydrogarnet*

The FTIR spectra (Fig. 5) show that siliceous hydrogarnet potentially precipitated in the blended cement pastes samples. As shown in Fig. 5 (a), the hydrated white cement paste presented the bands for O—H stretching in portlandite, CO_3 stretching in carbonation products and Si—O stretching of Q^1 and Q^2 tetrahedra within C-(A)-S-H at 3642 cm^{-1}, 1419–1409 cm^{-1} and 966–944 cm^{-1}, respectively [67]. The FTIR spectrum of fayalitic slag revealed the Si—O stretching band at 862 cm^{-1} attributed to the amorphous phase, along with bands at 827 cm^{-1} and 941 cm^{-1} corresponding to fayalite crystals [37,68]. In the blended white cement-fayalitic slag samples, the bands were associated with both the plain wPC paste and the fayalitic slag, and this was especially clear in samples with higher slag contents (i.e. 20FeO and 30FeO groups). The band at 862 cm^{-1} in the FTIR spectrum of anhydrous fayalitic slag decreases and another band at 872 cm^{-1} appears in the blended cement paste after hydration for 28 and 90 days. This band is positioned similarly to the band for CO_3 bending (873–872 cm^{-1}), but is much broader, as shown in Fig. 5 (b). The broad band at 872 cm^{-1} may be related to both CO_3 bending and Si—O stretching in siliceous hydrogarnet [69]. No characteristic ferrihydrite band (e.g. the Fe-OH band at ~1335 cm^{-1}) was identified.

The TG results (Fig. 6 (a)) indicate that the siliceous hydrogarnet in the hydrated cement paste after curing for 90 days could be predominantly Fe- rather than Al-bearing, since there is no prominent peak at ~300 °C in the derivative thermogravimetric (DTG) data that is typically associated with the decomposition of Al-bearing siliceous hydrogarnet [24]. The TG results of hydrated cement paste at other ages can be found in Fig. S2. Fe-bearing siliceous hydrogarnet synthesized at room temperature exhibits steady mass loss between 200 °C and 400 °C [24], which is what is observed here.

Fig. 6 (b) shows that hydration of fayalitic slag consumes $Ca(OH)_2$ and increases bound water content per gram of wPC, consistent with the QXRD results (Table S2). This increase in bound water was particularly pronounced in the 20FeO and 30FeO samples, primarily due to the pozzolanic reaction and the formation of more C-(A)-S-H per gram of

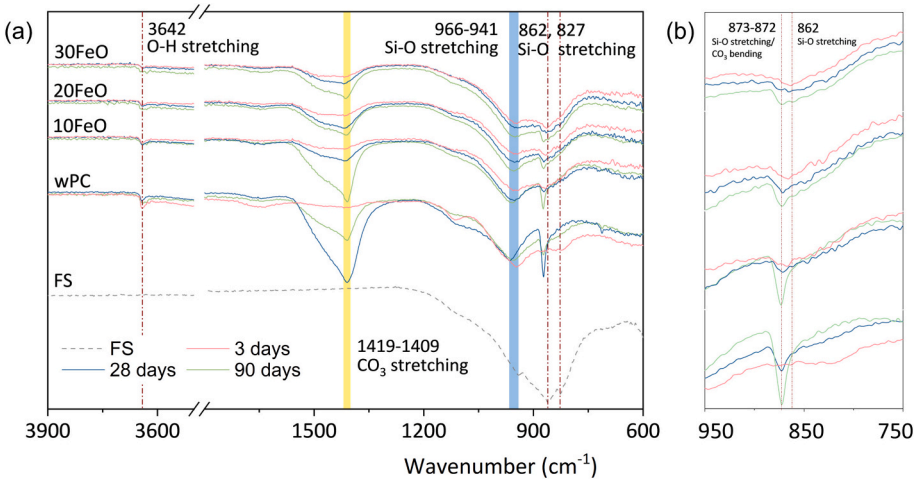

Fig. 5. FTIR spectra of hydrated cement paste and raw materials. (a) FTIR spectra of anhydrous fayalitic slag (FS), hydrated white cement paste (wPC) and blended cement paste (10FeO, 20FeO, 30FeO) after curing for 3, 28 and 90 days, (b) a close-up view of the FTIR spectra within wavenumber of 950–750 cm^{-1}.

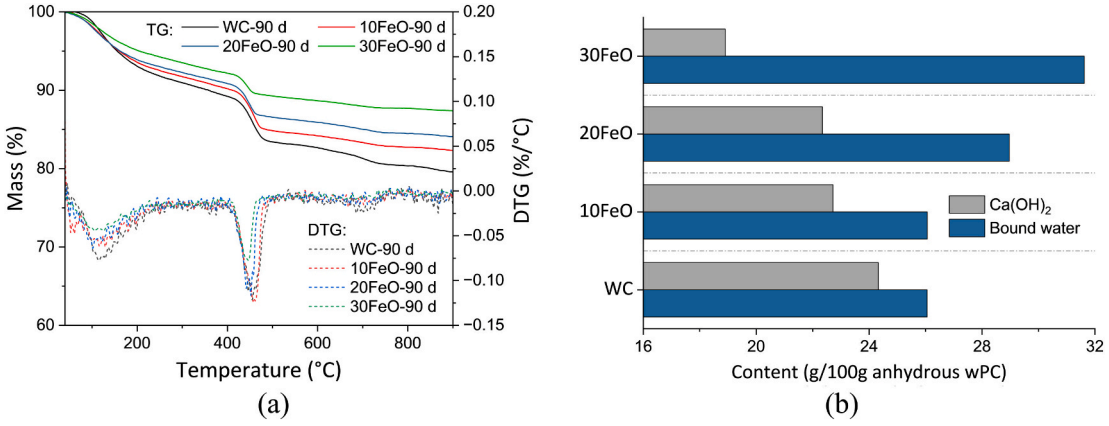

Fig. 6. TG analysis of cement paste after hydration for 90 days. (a) TG and derivative thermogravimetric (DTG) results; (b) calculated $Ca(OH)_2$ and bound water content based on the results shown in (a) and the tangential method (see Section 2.3).

wPC. The formation of Fe-bearing hydration products, such as Fe-siliceous hydrogarnet, may also contribute.

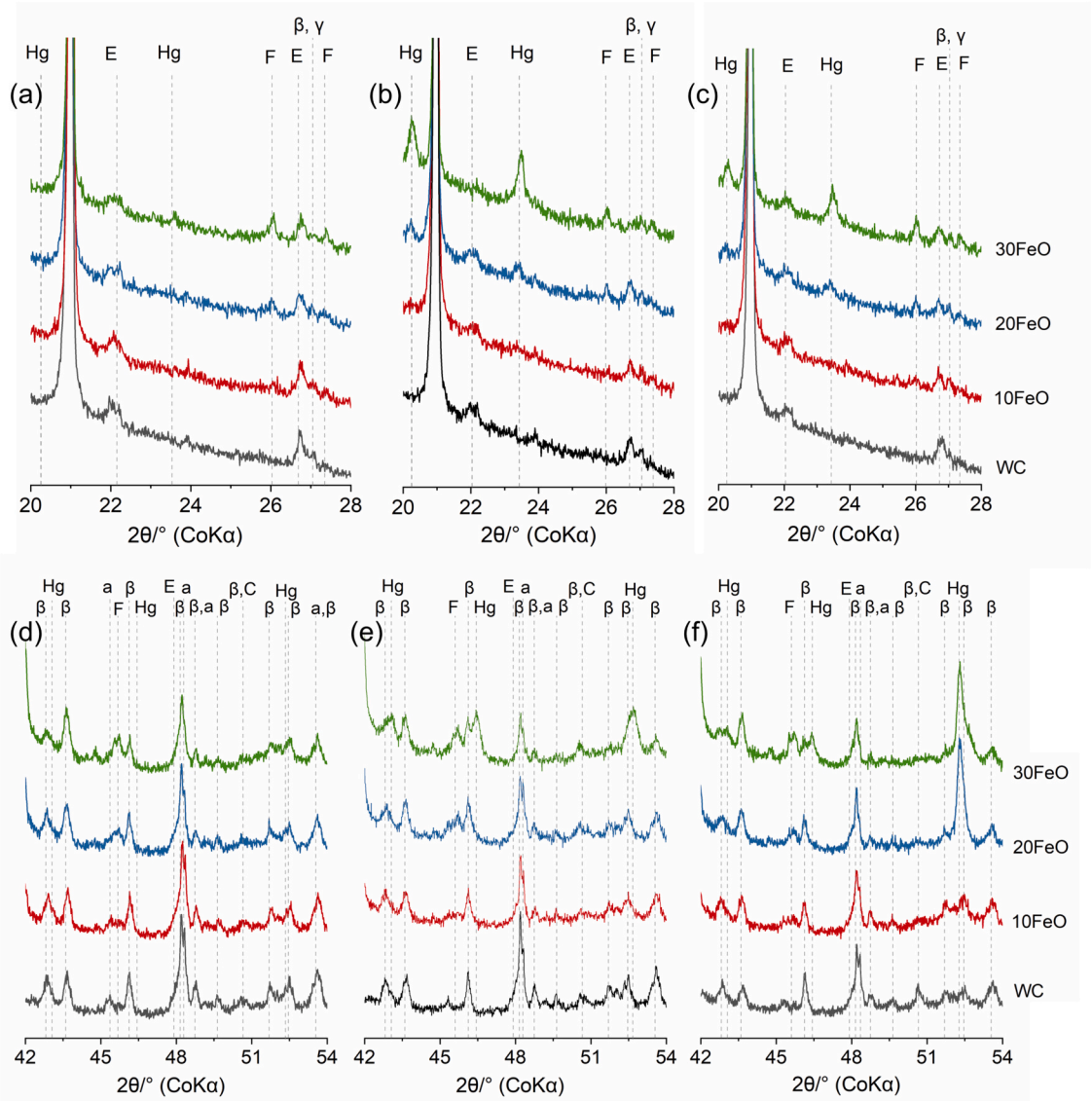

Fig. 7. XRD patterns of hydrated plain white cement paste and blended white cement-fayalitic slag paste focused on 2 different 2θ regions of interest. (a) 20–28° 2θ CoKα of samples after curing for 3 (a), 28 (b) and 90 (c) days respectively. (d-f) 42–54° 2θ CoKα of samples after curing for 3 (d), 28 (e) and 90 (f) days respectively. H: hydrogarnet, E: ettringite, F: fayalite, β: β-C_2S, γ: γ-C_2S, a: C_3S, C: calcite.

The XRD patterns (Fig. 7) show that Fe-siliceous hydrogarnet precipitated in the hydrated cement paste, which is identified by its characteristic peaks at 20.3°, 23.5°, 43.1°, 46.4°, and 52.3° 2θ CoKα. These peaks became prominent in the "20FeO" and "30FeO" samples at 28 and 90 days of hydration, especially the peak at 23.5°, which shows the crystallization of siliceous hydrogarnet at later stages, consistent with the FTIR results (Fig. 5). The XRD data also show precipitation of portlandite, C-(A)-S-H (amorphous hump), and ettringite (see full diffractograms in in Supporting Information S1, Fig. S3).

The estimated Fe-siliceous hydrogarnet contents in the samples studied here, calculated using Rietveld analysis, are presented in Table 6. Al-siliceous hydrogarnet was excluded from the QXRD calculations because (i) no peak for Al—Si hydrogarnet is present in the TGA results and (ii) mass balance results showed that the majority of Al was present in the C-(A)-S-H phase in slag-containing cement paste (see Table S3). No Fe-siliceous hydrogarnet was identified in plain wPC paste. In blended FS-wPC paste, the total content of Fe-siliceous hydrogarnet increased with hydration durations and higher fayalitic slag dosages. In the 10FeO samples (10 wt% amorphous FeO in the binder), the calculated Fe-siliceous hydrogarnet amount was low, reaching only 1.2 wt% after hydration for 90 days. It increased to above 1% after 3 days of hydration and rose to 2.95 wt% and 5.65 wt% for the 20FeO and 30FeO sample groups respectively after 90 days of hydration. The ratio of Fe-bearing silica-rich hydrogarnet ($Ca_3Fe_2(SiO_4)_{1.34}(OH)_{6.64}$) amount to the total Fe-siliceous hydrogarnet amount generally increased over time, which corresponds to increased dissolution of fayalitic slag with time.

Fe-siliceous hydrogarnet crystals were found on the surfaces of fayalitic slag particles under SEM-BSE, as illustrated in Fig. 8 (a-b), which were identified from their Ca-rich compositions and particulate morphology (Fayalitic slag has CaO content <1.4 wt%). They were assigned as Fe-siliceous hydrogarnet because the chemical composition cloud of data points for these crystals (Fig. 8 (c)) was far from those for the slag (fayalite crystal and bulk slag) and Fe-adsorbed C-(A)-S-H identified through BSE-EDS analysis. The lower Ca/Si but higher Fe/Si atomic ratios could be owing to intermixing with ferrihydrite. Furthermore, these crystals had nano-sized spherical morphology, consistent with the previously reported morphology of Fe-siliceous hydrogarnet [31,70].

3.3. Distributions of reacted Fe in hydration products

Fe K-edge XANES spectra of the fayalitic slag and the hydrated cement paste with slag are shown in Fig. 9. The pre-edge centroid observed at ~7112.8 eV is due to quadrupolar 1s→3d electronic transitions of Fe, suggesting the presence of Fe(II) and Fe(III) in the Fe-containing phases [71,72]. After hydration, the XANES spectra of cement paste showed a shoulder near 7114.1 eV in the pre-edge region, corresponding to Fe(III) compounds [28]. Moreover, the white-line positions of cement paste spectra shifted toward higher energies with hydration ages, indicating the partial oxidation of Fe(II) to Fe(III), which is consistent with the Mössbauer spectroscopy analysis (Fig. 2).

Extended X-ray absorption fine structure (EXAFS) multi-shell fitting (Fig. S4 and Table S4) reveals a progressive shortening of Fe—Si distances (Fe—Si_1 and Fe—Si_2 in Table S4) from 3 to 28 and 90 days of hydration, consistent with increasing structural ordering and incorporation of Fe into silicate hydrate environments such as Fe-siliceous hydrogarnet (Section 3.2.2) and Fe-adsorbed C-(A)-S-H (Section 3.2.1).

The Fe partitioning among various phases of hydrated cement paste was determined by LCF of the XANES spectra, as shown in Table 7 and Fig. S5. The Fe fraction in fayalitic slag generally decreased with curing ages, suggesting the reaction of Fe from the slag. The reacted Fe fraction was below 20%, consistent with the Mössbauer spectroscopy results (Fig. 2 and Table 4). The reaction degree was lower than the overall slag reaction degree estimated from XRD- PONKCS and BSE imaging analysis (S1.1, S1.2, Table S5), indicating Fe in the fayalitic slag could react more slowly than the Si.

Limited Fe was identified in the ferrihydrite phase within 28 days of hydration. Notably, although the inclusion of ferrihydrite in the combination fittings resulted in the lowest R-factor, comparable fits were obtained without this phase, indicating its presence cannot be reliably determined based on the LCF results. Furthermore, no experimental results from FTIR, TGA or XRD suggested the formation of ferrihydrite in this study.

The Fe proportions in Fe-siliceous hydrogarnet generally increased with hydration time (Tables 7 and 8), which is consistent with the XRD analysis (Fig. 7 and Table 6). Notably, the Fe proportions in Fe-siliceous hydrogarnet were all at 15–16% after hydration for 90 days, regardless of the fayalitic slag content in cement (Table 8). This contrasts with the earlier study that most reacted Fe was in the Fe-siliceous hydrogarnet phase after hydration for more than 1 day, because the Fe-adsorbed C-S-H phases were not included in the previous LCF calculations [23].

The relative amount of Fe in Fe(III)-adsorbed C-S-H also increased with curing age. Among all 28 and 90 day hydration products (Table 7), most of the Fe was in Fe(III)-adsorbed C-S-H, indicating its thermodynamic stability over other Fe-bearing hydration products in the white cement-fayalitic slag paste. Although the proportion of Fe in Fe(III)-adsorbed C-S-H varied with time, they stabilised within the range of 75–84% after 90 days of hydration (Table 8). These values could contain uncertainties as the reference spectra [29,30] were based on Fe-adsorbed C-S-H rather than C-(A)-S-H, which was formed in this study.

Reacted Fe was also identified in the Fe(II)-adsorbed C-S-H phase of blended cement paste with high slag content (36 and 54 wt% in binder). Except for the 3 day 30FeO cement paste sample, where the Fe(II)-adsorbed C-S-H was reliably identified in the LCF, comparable fits were obtained for the other samples without it, indicating its presence cannot be clearly determined beyond the 3-day 30FeO system. The Fe proportions in Fe(II)-adsorbed C-S-H were much lower than those in Fe(III)-adsorbed C-S-H (Tables 7 and 8), which verified the hypothesis that relatively high Fe/Si atomic ratios in C-(A)-S-H were primarily associated with Fe(III) adsorption (Section 3.2.1).

Table 6
Fe-siliceous hydrogarnet content determined by QXRD analysis. R_B denotes the R-Bragg factor. The full QXRD results are shown in Table S2.

Curing age (days)	Sample group	$Ca_3Fe_2(SiO_4)_{1.34}(OH)_{6.64}$ (wt%)	R_B	$Ca_3Fe_2(SiO_4)_{0.84}(OH)_{8.64}$ (wt%)	R_B	Total Fe-siliceous hydrogarnet (wt%)
3	WC	–	–	–	–	–
	10FeO	0.0 ± 0.02	2.4 ± 2.4	0.2 ± 0.03	3.7 ± 0.2	0.3 ± 0.05
	20FeO	0.4 ± 0.04	4.1 ± 2.3	0.6 ± 0.09	3.9 ± 0.7	1.0 ± 0.05
	30FeO	0.4 ± 0.14	4.6 ± 0.4	0.8 ± 0.53	3.6 ± 0.2	1.2 ± 0.39
28	WC	–	–	–	–	–
	10FeO	0.6 ± 0.12	6.5 ± 0.0	0.6 ± 0.21	4.8 ± 0.6	1.2 ± 0.09
	20FeO	1.0 ± 0.28	4.4 ± 0.7	1.0 ± 0.37	3.5 ± 0.6	1.9 ± 0.65
	30FeO	3.8 ± 1.50	3.1 ± 0.8	1.8 ± 1.03	2.5 ± 0.9	5.6 ± 2.53
90	WC	–	–	–	–	–
	10FeO	0.8 ± 0.21	7.4 ± 0.0	0.4 ± 0.17	5.4 ± 0.3	1.3 ± 0.05
	20FeO	1.2 ± 0.66	4.5 ± 0.6	1.8 ± 0.59	4.8 ± 1.9	3.0 ± 0.08
	30FeO	4.9 ± 0.62	2.9 ± 0.0	0.8 ± 0.51	2.6 ± 0.2	5.7 ± 1.18

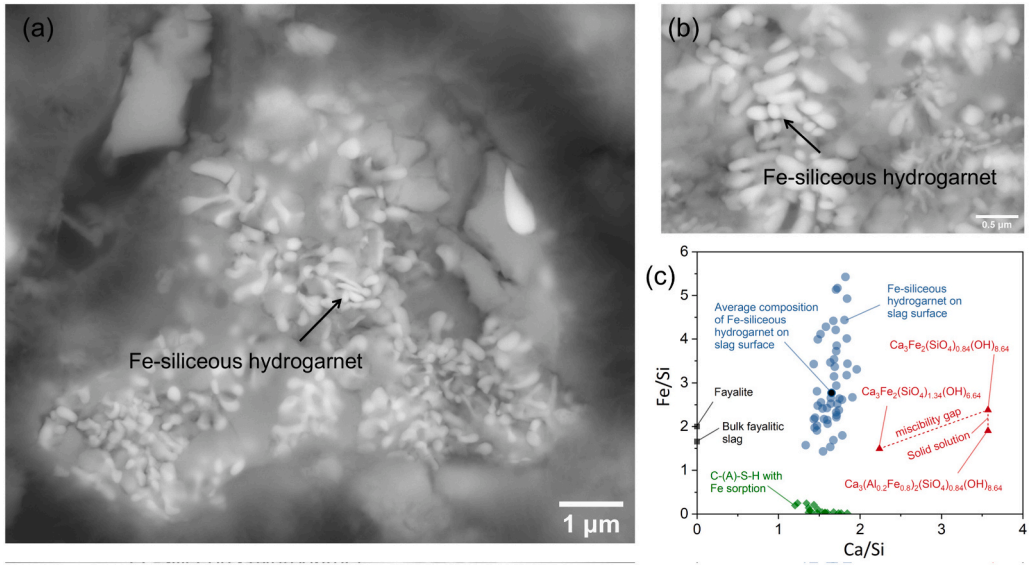

Fig. 8. Fe-siliceous hydrogarnet on the surface of fayalitic slag particle. (a-b) BSE images of the Fe-siliceous hydrogarnet; (c) Fe/Si and Ca/Si atomic ratios. a.

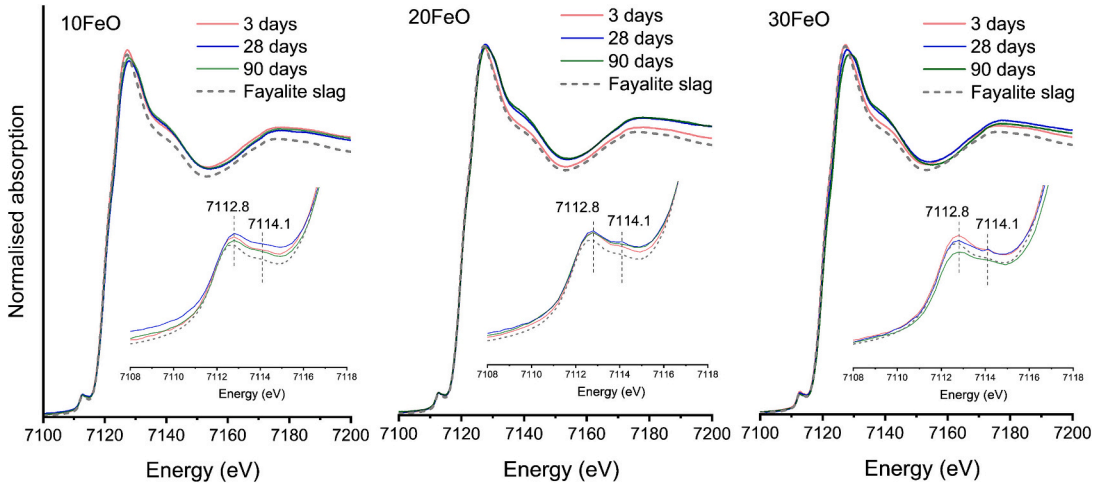

Fig. 9. Normalised Fe K-edge XANES spectra of fayalitic slag and cement paste with various slag contents and after curing for different ages. The insets show expanded views of the 1 s→3d pre-edge region.

Table 7
Fe partitioning in the Fe-bearing phases of hydrated cement paste determined by LCF of XANES spectra. Calculated uncertainties are given in parentheses.

Mixture	Curing age (days)	Fe speciation percentages (%)					R-factor
		Fayalitic slag	Fe-siliceous hydrogarnet	Fe(III)-adsorbed C-S-H	Ferrihydrite	Fe(II)-adsorbed C-S-H	
10FeO	3	96.6(0.10)	0.0(1.57)	3.4(0.88)	0.0(1.08)	–	6×10^{-5}
	28	89.1(0.30)	0.0(1.58)	6.6(0.99)	4.2(0.99)	–	1×10^{-4}
	90	90.4(0.29)	1.5(0.59)	7.9(0.59)	–	0.3(0.29)	7×10^{-5}
20FeO	3	97.2(0.10)	0.0(0.90)	2.3(0.60)	0.5(0.60)	–	2×10^{-5}
	28	92.5(0.39)	0.0(0.68)	6.9(0.68)	–	0.6(0.39)	1×10^{-4}
	90	90.7(0.20)	1.5(0.68)	7.8(0.68)	–	–	1×10^{-4}
30FeO	3	96.6(0.20)	0.0(0.59)	–	2.2(0.59)	1.2(0.20)	2×10^{-5}
	28	89.9(0.29)	1.4(0.49)	8.1(0.49)	–	0.7(0.29)	5×10^{-5}
	90	83.2(0.20)	2.6(0.39)	12.5(0.39)	–	1.7(0.20)	3×10^{-5}

3.4. Thermodynamic modelling

As portlandite and C-(A)-S-H were the main hydration products (Figs. 7 and S3), thermodynamic modelling was performed on a line from fayalitic slag to portlandite-dominated hydration products, as shown in Fig. 10 (a), and another line from the C-(A)-S-H dominated area through fayalitic slag to the other side, as shown in Fig. 10 (d).

Here the fayalitic slag-cement paste interface was separated into three regions: (I) unhydrated slag particle, (II) outer surface of slag, (III) hydrated cement paste, according to the assumptions introduced in Section 2.4 and the mass percentages determined by EDS line analysis, as illustrated in Fig. 10 (b, e).

Table 8
Distributions of Fe in the hydration products of cement paste, calculated based on the LCF results in Table 7. Calculated uncertainties are given in parentheses.

Mixture	Curing age (days)	Distributions of Fe species in the hydration products (%)			
		Fe-siliceous hydrogarnet	Fe(III)-adsorbed C-S-H	Ferrihydrite	Fe(II)-adsorbed C-S-H
10FeO	3	0.0(45.71)	100.0 (28.57)	0.0(31.43)	–
	28	0.0(14.55)	60.9 (10.75)	39.1(10.16)	–
	90	15.3(6.59)	81.6(8.62)	–	3.1(3.15)
20FeO	3	0.0(32.14)	82.1 (24.36)	17.9(22.07)	–
	28	0.0(9.09)	92.2 (13.88)	–	7.8(5.60)
	90	15.8(7.70)	84.2(9.14)	–	–
30FeO	3	0.0(17.65)	–	64.7(21.45)	35.3(7.96)
	28	13.6(5.25)	79.6(7.17)	–	6.8(3.11)
	90	15.3(2.53)	74.7(3.23)	–	10.0(1.29)

Under both conditions, the thermodynamic modelling results revealed the Fe-bearing hydration products were Fe-siliceous hydrogarnet, ferrihydrite, and Fe adsorbed C-(A)-S-H (Fig. 10 (c) and (f)), in agreement with the experimental observations (Section 3.2).

The Fe siliceous hydrogarnet and ferrihydrite phases were mainly formed at the interface between regions II and III (Fig. 10 (c) and (f)), consistent with the microscopic observation in Fig. 8. Their contents dramatically declined beyond ~1 μm from the slag surface owing to the reduced Fe content in the cement matrix, suggesting the limited content and restricted locations favourable to formation of these phases. Given the intermixing between the fayalitic slag and the cement paste at the interface during EDS analysis (Fig. 10 (c) and (f)), the actual content of Fe siliceous hydrogarnet and ferrihydrite phases at the interface is likely lower than that predicted by the thermodynamic modelling. As the content of these two phases decreased to ~0, Fe was mainly incorporated into the Fe adsorbed C-(A)-S-H phase. This agrees with the XANES LCF results (Tables 7 and 8), which showed that most of the reacted Fe is in the Fe(III)-adsorbed C-S-H phase.

4. Discussion

This study quantified a significant partitioning of Fe adsorbed on the C-(A)-S-H phase (Tables 5, 7 and 8) in Portland cement paste, especially Fe(III) adsorption on outer C-(A)-S-H, which is often overlooked in previous studies of Fe hydration [15,23,73]. The Fe-adsorbed C-(A)-S-H phase was stable until 90 days of hydration, potentially due to the Fe incorporation into the interlayer structure of C-(A)-S-H phases [29]. The Fe/Si atomic ratios generally increased with decreasing Ca/Si atomic ratios, especially for the outer C-(A)-S-H (Fig. S6). Previous studies [29,30] have indicated that Fe adsorption on C-S-H increased linearly with Fe concentrations, irrespective of Ca/Si atomic ratios and solution pH. Hence, the reduction in Ca/Si atomic ratios could suggest a higher total dissolved slag content, which increased Fe concentrations and thereby enhanced the Fe adsorption on C-(A)-S-H.

Fe-siliceous hydrogarnet was another stable phase identified at the fayalitic slag surface (Figs. 7 and 8), particularly after hydration for 90 days. Prior research has also reported its slow formation kinetics (~years) in Portland cement systems [23,24,74]. Given the increasing Fe fractions in Fe-siliceous hydrogarnet with curing age (Table 8), it is plausible this phase will continue to incorporate Fe with prolonged hydration, which deserves to be studied in the future.

Fe-bearing hydration products identified in this study are mainly Fe

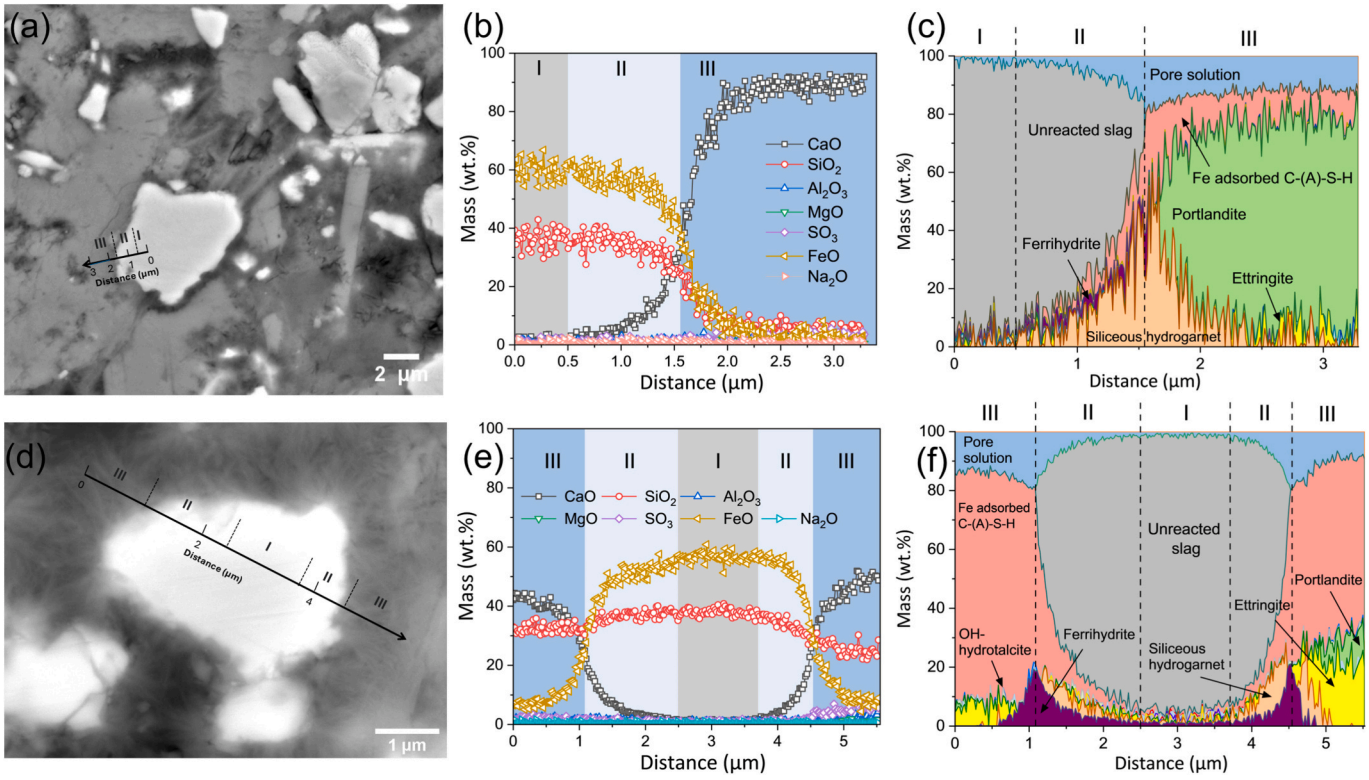

Fig. 10. Thermodynamic modelling based on chemical compositions determined by EDS line analysis. (a) Line for EDS analysis on a BSE image of a "20FeO" group sample after hydration for 28 days, the arrow denotes the direction of EDS analysis; (b) chemical compositions of the points on line in (a); (c) phase assemblage predicted by thermodynamic modelling on the line in (a); (d) line for EDS analysis on a BSE image of a "30FeO" group sample after hydration for 90 days, the arrow denotes the direction of EDS analysis; (e) chemical compositions of the points on line in (d); (f) phase assemblage predicted by thermodynamic modelling on the line in (d). **I**: unhydrated slag particle; **II**: outer surface of slag; **III**: hydrated cement paste.

(III)-containing phases (i.e. Fe(III)-adsorbed C-(A)-S-H and Fe-siliceous hydrogarnet) rather than Fe(II)-containing phases, indicating the oxidation of Fe(II) from the fayalitic slag. Although the samples were cured under N_2, oxygen may still have been introduced through dissolved oxygen in the tap water and entrapped air during cement paste preparation. In addition, the high pH of cement paste pore solution could also promote Fe(II) oxidation [75]. As neither water degassing nor vacuum mixing is commonly applied for preparation of cement-based materials, this research suggests that Fe(II) oxidation can occur even in oxygen-limited environments (e.g. the interior of high-strength concrete) during service life. Moreover, despite completing the hydration stoppage procedure (described in Section 2.2) within 1 h, exposure to air during this procedure may have also contributed to Fe(II) oxidation (<6%), potentially leading to an underestimation of Fe(II)-containing hydration products.

The synthetic fayalitic slag used in this study consists of FeO and SiO_2, whereas industrial fayalitic slag can have more complex chemistries, for example containing CaO and Al_2O_3 [8,76]. Variations in slag chemistry can influence the speciation of Fe in the hydration products of Portland cement system. For instance, changes in contents of CaO and SiO_2 in the slag could promote the formation of Fe-siliceous hydrogarnet and alter the Ca/Si atomic ratios of C-(A)-S-H, leading to different Fe adsorption mechanisms (e.g. interlayer bonding and formation of a separate cluster) on C-(A)-S-H [29,30]. In addition, a high alumina content in slag amorphous phase could promote the precipitation in mossbauerite-like LDH phases [34,35]. To better understand Fe chemistry in Portland cement system blended with Fe-rich slag of varying compositions, it is essential to establish a comprehensive thermodynamic database for the Fe-containing phases that are not currently included in Cemdata18 [55,77,78], such as Fe-adsorbed C-(A)-S-H and Fe(II)/Fe(III)-containing LDH phases.

To further utilise the reactive Fe in Fe-rich slags for improving cement performance, the formation of Fe-containing hydration products could be further engineered. Fe-rich ettringite has been demonstrated to improve the sulfate resistance of Portland cement-based concrete [79,80], whilst the effects of Fe-adsorbed C-(A)-S-H and Fe-siliceous hydrogarnet on concrete performance, such as the compressive strength (Table S6), remain largely unclear [81,82]. There is therefore a need for further research to understand the effects of this Fe speciation (Fe adsorption on C-(A)-S-H and Fe-siliceous hydrogarnet) on concrete performance. Another direction for future research can be to understand the effects of modifying the chemistry of Fe-containing cement to promote Fe-rich ettringite formation over other Fe-bearing phases.

5. Conclusions

This study investigated the reaction and speciation of Fe in blended white Portland cement-fayalitic slag paste with varying slag content and hydration durations. The reacted Fe was identified in Fe-siliceous hydrogarnet and Fe-adsorbed C-(A)-S-H phases, with possible incorporation into ferrihydrite phase. The ferrihydrite phase might form but subsequently destabilise within the 28 days of hydration period. Conversely, Fe partitioning of Fe-siliceous hydrogarnet and Fe-adsorbed C-(A)-S-H phases increased with hydration time. Among these phases, the Fe(III)-adsorbed C-(A)-S-H phase contained the most reacted Fe across all slag content. Thermodynamic modelling results suggested that ferrihydrite and Fe-siliceous hydrogarnet were confined to the slag/cement paste interfaces, whereas Fe-adsorbed C-(A)-S-H was the main Fe-containing phase at the hydrated white cement paste region, consistent with the experimental observations.

These findings provide fundamental insights into Fe hydration and phase assemblage in the Portland cement paste environment, advancing the understanding of the Fe speciation upon hydration.

CRediT authorship contribution statement

Jianhang Feng: Writing – review & editing, Writing – original draft, Methodology, Investigation, Formal analysis. **Minggen Zhang:** Writing – review & editing, Investigation. **James Eales:** Writing – original draft, Methodology, Investigation. **Siyi Shen:** Investigation. **Marcus Yio:** Writing – review & editing, Investigation. **Thokozile Kathyola:** Writing – review & editing, Methodology, Investigation, Formal analysis. **Yiannis Pontikes:** Writing – review & editing, Resources. **Paul A. Bingham:** Resources. **Rupert J. Myers:** Writing – review & editing, Supervision, Funding acquisition, Formal analysis.

Declaration of competing interest

The authors declare that they have no known competing financial interests or personal relationships that could have appeared to influence the work reported in this paper.

Acknowledgements

The research leading to this publication benefitted from EPSRC grants EP/W026104/1, EP/R010161/1 and EP/R017727/1, and EP/Y001370/1 (selected by the European Research Council (ERC) for a Starting Grant, funded by the EPSRC Frontier Research Guarantee) and the European Union's Horizon 2020 Programme (H2020/2014-2020) under grant agreement no. 958208. The authors thank Christina Siakati for synthesising the fayalitic slag samples and Fabio Furcas for synthesising the 6-line and siliceous ferrihydrite samples.

Appendix A. Supplementary data

Supplementary data to this article can be found online at https://doi.org/10.1016/j.cemconres.2026.108324.

Data availability

Data will be made available on request.

References

[1] J.G. Driver, E. Bernard, P. Patrizio, P.S. Fennell, K. Scrivener, R.J. Myers, Global decarbonization potential of CO_2 mineralization in concrete materials, Proc. Natl. Acad. Sci. 121 (2024) e2313475121.
[2] S.-M. Jian, B. Wu, Compressive behavior of compound concrete containing demolished concrete lumps and recycled aggregate concrete, Construct. Build Mater. 272 (2021) 121624.
[3] L.D. Ellis, A.F. Badel, M.L. Chiang, R.J.-Y. Park, Y.-M. Chiang, Toward electrochemical synthesis of cement—an electrolyzer-based process for decarbonating $CaCO_3$ while producing useful gas streams, Proc. Natl. Acad. Sci. 117 (2020) 12584–12591.
[4] J. Feng, Y. Wang, S. Shen, R.J. Myers, Wet carbonation and stabilities of Fe (II)-containing materials, Cem. Concr. Compos. 106217 (2025).
[5] M.C. Juenger, R. Snellings, S.A. Bernal, Supplementary cementitious materials: new sources, characterization, and performance insights, Cem. Concr. Res. 122 (2019) 257–273.
[6] B. Lu, Z. Li, M. Li, J. Feng, T.N. Wong, S. Qian, Substitution of cement by marine clay in spray-based 3D concrete printing, J. Sustain. Cem.-Based Mater. 13 (2024) 375–388.
[7] D. Meng, P. Jeevaganth, J. Feng, B. Lu, Z. Li, S. Qian, MgO activated calcined marine clay and its carbonation, J. Sustain. Cem.-Based Mater. 13 (2024) 1596–1610.
[8] A. Peys, V. Isteri, J. Yliniemi, P.N. Lemougna, C. Utton, J.L. Provis, R. Snellings, T. Hanein, Sustainable iron-rich cements: raw material sources and binder types, Cem. Concr. Res. 157 (2022) 106834.
[9] H.J. Qureshi, J. Ahmad, A. Majdi, M.U. Saleem, A.F. Al Fuhaid, M. Arifuzzaman, A study on sustainable concrete with partial substitution of cement with red mud: a review, Materials 15 (2022) 7761.
[10] W. Tang, Z. Wang, Y. Liu, H. Cui, Influence of red mud on fresh and hardened properties of self-compacting concrete, Construct. Build Mater. 178 (2018) 288–300.
[11] M. Ghalehnovi, N. Roshan, E. Hakak, E.A. Shamsabadi, J. de Brito, Effect of red mud (bauxite residue) as cement replacement on the properties of self-compacting concrete incorporating various fillers, J. Clean. Prod. 240 (2019) 118213.

[12] V. Hallet, High-Volume Replacement of Cement by Non-ferrous-Metallurgy Slag and Impact of Limestone, Fineness and Grinding Aids, Ghent University, 2022.
[13] V. Hallet, Y. Pontikes, N. De Belie, Valorisation of iron-rich non-ferrous metallurgy slag in concrete and effects on durability, in: ISSSI 2023, 2023.
[14] M. Giels, T. Hertel, T.N. Nguyen, Y. Pontikes, Bringing metallurgy and cement industry closer: Fe-rich glass as a supplementary cementitious material, J. Sustain. Metall. 11 (2025) 2236–2255.
[15] M. Wenzel, F. Georget, T. Matschei, From bauxite residue mineralogy to reactivity and properties of blended cements, Cem. Concr. Res. 192 (2025) 107854.
[16] M. Giels, T. Hertel, K. Gijbels, W. Schroeyers, Y. Pontikes, High performance mortars from vitrified bauxite residue; the quest for the optimal chemistry and processing conditions, Cem. Concr. Res. 155 (2022) 106739.
[17] X. Sun, J. Liu, Y. Zhao, J. Zhao, Z. Li, Y. Sun, J. Qiu, P. Zheng, Mechanical activation of steel slag to prepare supplementary cementitious materials: a comparative research based on the particle size distribution, hydration, toxicity assessment and carbon dioxide emission, J. Build. Eng. 60 (2022) 105200.
[18] B. Huo, B. Li, C. Chen, Y. Zhang, Surface etching and early age hydration mechanisms of steel slag powder with formic acid, Construct. Build Mater. 280 (2021) 122500.
[19] C.F. Dunant, S. Joseph, R. Prajapati, J.M. Allwood, Electric recycling of Portland cement at scale, Nature (2024) 1–7.
[20] T. Hertel, Y. Pontikes, Geopolymers, inorganic polymers, alkali-activated materials and hybrid binders from bauxite residue (red mud)–putting things in perspective, J. Clean. Prod. 258 (2020) 120610.
[21] G. Möschner, B. Lothenbach, F. Winnefeld, A. Ulrich, R. Figi, R. Kretzschmar, Solid solution between Al-ettringite and Fe-ettringite ($Ca_6[Al_{1-x}Fe_x(OH)_6]_2(SO_4)_3 \cdot 26H_2O$), Cem. Concr. Res. 39 (2009) 482–489.
[22] B. Dilnesa, B. Lothenbach, G. Le Saout, G. Renaudin, A. Mesbah, Y. Filinchuk, A. Wichser, E. Wieland, Iron in carbonate containing AFm phases, Cem. Concr. Res. 41 (2011) 311–323.
[23] B. Dilnesa, E. Wieland, B. Lothenbach, R. Dähn, K. Scrivener, Fe-containing phases in hydrated cements, Cem. Concr. Res. 58 (2014) 45–55.
[24] B.Z. Dilnesa, B. Lothenbach, G. Renaudin, A. Wichser, D. Kulik, Synthesis and characterization of hydrogarnet $Ca_3(Al_xFe_{1-x})_2(SiO_4)_y(OH)_{4(3-y)}$, Cem. Concr. Res. 59 (2014) 96–111.
[25] K. Rozov, U. Berner, C. Taviot-Gueho, F. Leroux, G. Renaudin, D. Kulik, L. W. Diamond, Synthesis and characterization of the LDH hydrotalcite–pyroaurite solid-solution series, Cem. Concr. Res. 40 (2010) 1248–1254.
[26] K. Rozov, H. Curtius, A. Neumann, D. Bosbach, Synthesis, characterization and stability properties of Cl-bearing hydrotalcite-pyroaurite solids, Radiochim. Acta 101 (2013) 101–110.
[27] M. Zhang, E. Bernard, M. Yio, C. Cheeseman, R. Myers, Formation of sodium iron silicate hydrate (NFSH) in Fe-rich cementitious systems, Cem. Concr. Res. 205 (2026) 108241.
[28] F.E. Furcas, S. Mundra, B. Lothenbach, C.N. Borca, T. Huthwelker, U.M. Angst, The influence of silicon on the formation and transformation of corrosion products, Cem. Concr. Res. 182 (2024) 107554.
[29] A. Mancini, E. Wieland, G. Geng, R. Dähn, J. Skibsted, B. Wehrli, B. Lothenbach, Fe (III) uptake by calcium silicate hydrates, Appl. Geochem. 113 (2020) 104460.
[30] A. Mancini, E. Wieland, G. Geng, B. Lothenbach, B. Wehrli, R. Dähn, Fe (II) interaction with cement phases: method development, wet chemical studies and X-ray absorption spectroscopy, J. Colloid Interface Sci. 588 (2021) 692–704.
[31] J. Siramanont, B.J. Walder, L. Emsley, P. Bowen, Iron incorporation in synthetic precipitated calcium silicate hydrates, Cem. Concr. Res. 142 (2021) 106365.
[32] J. Astoveza, R. Trauchessec, S. Migot-Choux, R. Soth, Y. Pontikes, Iron-rich slag addition in ternary binders of Portland cement, aluminate cement and calcium sulfate, Cem. Concr. Res. 153 (2022) 106689.
[33] J. Astoveza, R. Trauchessec, R. Soth, Y. Pontikes, Properties of calcium aluminate blended cement incorporating iron-rich slag: evolution over a curing period of 1 year, Construct. Build Mater. 282 (2021) 122569.
[34] V. Hallet, M.T. Pedersen, B. Lothenbach, F. Winnefeld, N. De Belie, Y. Pontikes, Hydration of blended cement with high volume iron-rich slag from non-ferrous metallurgy, Cem. Concr. Res. 151 (2022) 106624.
[35] V. Hallet, M.T. Pedersen, B. Lothenbach, F. Winnefeld, L. Eykens, N. De Belie, Y. Pontikes, The hydration of ternary blended cements with Fe-rich slag from non-ferrous metallurgy and limestone, Cem. Concr. Res. 169 (2023) 107155.
[36] Y. Feng, Q. Yang, Q. Chen, J. Kero, A. Andersson, H. Ahmed, F. Engström, C. Samuelsson, Characterization and evaluation of the pozzolanic activity of granulated copper slag modified with CaO, J. Clean. Prod. 232 (2019) 1112–1120.
[37] C. Siakati, A.P. Douvalis, P. Ziogas, A. Peys, Y. Pontikes, Impact of the solidification path of FeOx–SiO2 slags on the resultant inorganic polymers, J. Am. Ceram. Soc. 103 (2020) 2173–2184.
[38] J. Feng, S. Joseph, M. Yang, T. Jantzen, K. Hack, R. Prajapati, Z. Li, C.F. Dunant, R. J. Myers, Speciation of Mn in electric arc furnace clinker, Cem. Concr. Res. 203 (2026) 108162.
[39] P.T. Teo, S.K. Zakaria, S.Z. Salleh, M.A.A. Taib, N. Mohd Sharif, A. Abu Seman, J. J. Mohamed, M. Yusoff, A.H. Yusoff, M. Mohamad, Assessment of electric arc furnace (EAF) steel slag waste's recycling options into value added green products: a review, Metals 10 (2020) 1347.
[40] R. Roy, T. Hertel, G. Pilla, Y. Pontikes, Revealing the hydration mechanisms in iron-rich calcium sulfoaluminate cements with elevated bauxite residue content, Construct. Build Mater. 449 (2024) 138495.
[41] R. Snellings, J. Chwast, Ö. Cizer, N. De Belie, Y. Dhandapani, P. Durdzinski, J. Elsen, J. Haufe, D. Hooton, C. Patapy, RILEM TC-238 SCM recommendation on hydration stoppage by solvent exchange for the study of hydrate assemblages, Mater. Struct. 51 (2018) 1–4.
[42] D. Jansen, C. Stabler, F. Goetz-Neunhoeffer, S. Dittrich, J. Neubauer, Does ordinary Portland cement contain amorphous phase? A quantitative study using an external standard method, Powder Diffract. 26 (2011) 31–38.
[43] G. Le Saoût, V. Kocaba, K. Scrivener, Application of the Rietveld method to the analysis of anhydrous cement, Cem. Concr. Res. 41 (2011) 133–148.
[44] R. Young, Introduction to the Rietveld method, The Rietveld Method (1993) 1–38.
[45] H. Wong, N. Buenfeld, Patch microstructure in cement-based materials: fact or artefact? Cem. Concr. Res. 36 (2006) 990–997.
[46] M.M. Australia, Intensity basics, energy dispersive spectroscopy, Myscope Microscopy Training, 2022.
[47] J. Rossen, K. Scrivener, Optimization of SEM-EDS to determine the C–A–S–H composition in matured cement paste samples, Mater Charact 123 (2017) 294–306.
[48] R. Meads, B. Place, F. Woodhams, R. Clark, The effect of absorber thickness in measurement of quadrupole splitting in a Mössbauer experiment, Nucl. Inst. Methods 98 (1972) 29–35.
[49] P. Sarma, V. Prakash, K. Tripathi, Optimization of the absorber thickness for improving the quality of a Mössbauer spectrum, Nucl. Inst. Methods 178 (1980) 167–171.
[50] K. Lagarec, D.G. Rancourt, Recoil-Mössbauer Spectral Analysis Software for Windows 43, University of Ottawa, Ottawa, ON, 1998.
[51] A. Dent, G. Cibin, S. Ramos, A. Smith, S. Scott, L. Varandas, M. Pearson, N. Krumpa, C. Jones, P. Robbins, B18: A core XAS spectroscopy beamline for Diamond, in: Journal of Physics: Conference Series, IOP Publishing, 2009, p. 012039.
[52] B. Ravel, M. Newville, ATHENA, ARTEMIS, HEPHAESTUS: data analysis for X-ray absorption spectroscopy using IFEFFIT, Synchrotron Radiat. 12 (2005) 537–541.
[53] D.A. Kulik, T. Wagner, S.V. Dmytrieva, G. Kosakowski, F.F. Hingerl, K. V. Chudnenko, U.R. Berner, GEM-Selektor geochemical modeling package: revised algorithm and GEMS3K numerical kernel for coupled simulation codes, Comput. Geosci. 17 (2013) 1–24.
[54] T. Thoenen, W. Hummel, U. Berner, E. Curti, The PSI/Nagra Chemical Thermodynamic Database 12/07, 2014.
[55] B. Lothenbach, D.A. Kulik, T. Matschei, M. Balonis, L. Baquerizo, B. Dilnesa, G. D. Miron, R.J. Myers, Cemdata18: a chemical thermodynamic database for hydrated Portland cements and alkali-activated materials, Cem. Concr. Res. 115 (2019) 472–506.
[56] R.J. Myers, S.A. Bernal, J.L. Provis, A thermodynamic model for C-(N-) ASH gel: CNASH_ss. Derivation and validation, Cem. Concr. Res. 66 (2014) 27–47.
[57] G.J. Long, D. Hautot, Q.A. Pankhurst, D. Vandormael, F. Grandjean, J.P. Gaspard, V. Briois, T. Hyeon, K.S. Suslick, Mössbauer-effect and x-ray-absorption spectral study of sonochemically prepared amorphous iron, Phys. Rev. B 57 (1998) 10716.
[58] G. Collins, T. Kachnowski, N. Benczer-Koller, M. Pasternak, Application of the Mössbauer effect to the characterization of an amorphous tin-oxide system, Phys. Rev. B 19 (1979) 1369.
[59] A. Peys, A.P. Douvalis, V. Hallet, H. Rahier, B. Blanpain, Y. Pontikes, Inorganic polymers from CaO-FeO_x-SiO_2 slag: the start of oxidation of Fe and the formation of a mixed valence binder, Front. Mater. 6 (2019) 212.
[60] S.J. Oh, D.C. Cook, Mössbauer effect determination of relative recoilless fractions for iron oxides, J. Appl. Phys. 85 (1999) 329–332.
[61] B.Z. Dilnesa, B. Lothenbach, G. Renaudin, A. Wichser, E. Wieland, Stability of monosulfate in the presence of iron, J. Am. Ceram. Soc. 95 (2012) 3305–3316.
[62] F. Avet, K. Scrivener, Investigation of the calcined kaolinite content on the hydration of Limestone Calcined Clay Cement (LC3), Cem. Concr. Res. 107 (2018) 124–135.
[63] Y. Feng, Q. Zhang, Q. Chen, D. Wang, H. Guo, L. Liu, Q. Yang, Hydration and strength development in blended cement with ultrafine granulated copper slag, PloS One 14 (2019) e0215677.
[64] F.E. Furcas, B. Lothenbach, O.B. Isgor, S. Mundra, Z. Zhang, U.M. Angst, Solubility and speciation of iron in cementitious systems, Cem. Concr. Res. 151 (2022) 106620.
[65] E.H. Oelkers, J. Schott, J.-L. Devidal, The effect of aluminum, pH, and chemical affinity on the rates of aluminosilicate dissolution reactions, Geochim. Cosmochim. Acta 58 (1994) 2011–2024.
[66] C.M. Santelli, S.A. Welch, H.R. Westrich, J.F. Banfield, The effect of Fe-oxidizing bacteria on Fe-silicate mineral dissolution, Chem. Geol. 180 (2001) 99–115.
[67] R. Ylmén, U. Jäglid, B.-M. Steenari, I. Panas, Early hydration and setting of Portland cement monitored by IR, SEM and Vicat techniques, Cem. Concr. Res. 39 (2009) 433–439.
[68] M. Scott, B. Downs, Fayalite, RRUFF, 2015.
[69] M.U. Okoronkwo, F.P. Glasser, Compatibility of hydrogarnet, $Ca_3Al_2(SiO_4)_x(OH)_{4(3-x)}$, with sulfate and carbonate-bearing cement phases: 5–85 C, Cem. Concr. Res. 83 (2016) 86–96.
[70] Y. Fang, K. Zhuang, H. Cui, Z. Zhang, A. Wang, C. Wang, D. Zheng, X. Wang, The state of Fe^{3+} in the C–F–A–S–H system with varying Fe/Si and Ca/Si ratios, J. Mater. Chem. A 11 (2023) 26193–26211.
[71] F. De Groot, High-resolution X-ray emission and X-ray absorption spectroscopy, Chem. Rev. 101 (2001) 1779–1808.
[72] M. Wilke, F. Farges, P.-E. Petit, G.E. Brown Jr., F. Martin, Oxidation state and coordination of Fe in minerals: an Fe K-XANES spectroscopic study, Am. Mineral. 86 (2001) 714–730.
[73] R. Roy, T. Hertel, C. Rößler, Y. Pontikes, Exploring the hydration potential and kinetics of Na-Ye'elimite and Ti-ferrite solid solutions, Cem. Concr. Res. 199 (2026) 108046.

[74] R. Taylor, I. Richardson, R. Brydson, Composition and microstructure of 20-year-old ordinary Portland cement–ground granulated blast-furnace slag blends containing 0 to 100% slag, Cem. Concr. Res. 40 (2010) 971–983.
[75] F. Furcas, B. Lothenbach, S. Mundra, O.B. Isgor, M.R. Geiker, U.M. Angst, Thermodynamic modeling: success in cement science–untapped potential in corrosion research, RILEM Tech. Lett. 10 (2025) 1–14.
[76] C. Siakati, A.P. Douvalis, V. Hallet, A. Peys, Y. Pontikes, Influence of CaO/FeO ratio on the formation mechanism and properties of alkali-activated Fe-rich slags, Cem. Concr. Res. 146 (2021) 106466.
[77] G.D. Miron, D.A. Kulik, Y. Yan, J. Tits, B. Lothenbach, Extensions of CASH+ thermodynamic solid solution model for the uptake of alkali metals and alkaline earth metals in CSH, Cem. Concr. Res. 152 (2022) 106667.
[78] D.A. Kulik, G.D. Miron, B. Lothenbach, A structurally-consistent CASH+ sublattice solid solution model for fully hydrated CSH phases: thermodynamic basis, methods, and Ca-Si-H_2O core sub-model, Cem. Concr. Res. 151 (2022) 106585.
[79] M.P. Pineyro, F.R. Steindl, I. Galan, A.C.M. Soares, F. Mittermayr, How siderite ($FeCO_3$) enhances the sulfate resistance of cementitious systems, Cem. Concr. Res. 199 (2026) 108010.
[80] F. Mittermayr, F. Steindl, M.P. Pineyro, L. Briendl, M. Sakoparnig, I. Galan, Exploring natural siderite ($FeCO_3$) as a novel supplementary cementitious material, Cem. Concr. Res. 197 (2025) 107975.
[81] A. Kaja, K. Schollbach, S. Melzer, S. Van Der Laan, H. Brouwers, Q. Yu, Hydration of potassium citrate-activated BOF slag, Cem. Concr. Res. 140 (2021) 106291.
[82] N. Noguchi, K. Siventhirarajah, T. Chabayashi, H. Kato, T. Nawa, Y. Elakneswaran, Hydration of ferrite-rich Portland cement: evaluation of Fe-hydrates and Fe uptake in calcium-silicate-hydrates, Construct. Build Mater. 288 (2021) 123142.